Construction and Building Materials 154 (2017) 1207–1215

Contents lists available at ScienceDirect

Construction and Building Materials

journal homepage: www.elsevier.com/locate/conbuildmat

Virtual Special Issue
Ground-Penetrating Radar and Complementary Non-Destructive Testing Techniques in Civil Engineering

Time-frequency analysis of air-coupled GPR data for identification of delamination between pavement layers

Hai Liu [a,b], Zhihao Deng [b], Feng Han [b,*], Yuanyou Xia [c], Qing Huo Liu [d], Motoyuki Sato [e]

[a] School of Civil Engineering, Guangzhou University, Guangzhou 510006, China
[b] Institute of Electromagnetics and Acoustics & Department of Electronic Science, Xiamen University, Xiamen 361005, China
[c] School of Civil Engineering and Architecture, Wuhan University of Technology, Wuhan 430070, China
[d] Department of Electrical and Computer Engineering, Duke University, NC 27708-0291, USA
[e] Center for Northeast Asian Studies, Tohoku University, Sendai 980-8576, Japan

HIGHLIGHTS

- STFT is used to analyze the instantaneous spectrum of composite GPR reflection.
- 3D GPR simulations is conducted using the Green's function method.
- A thin delamination cause the spectrum peak to shift towards a higher frequency.
- Reason of the occurrence of multiple spectrum peaks and their shift is explained.
- Laboratory experiments confirm the numerical results.

ARTICLE INFO

Article history:
Received 23 November 2016
Received in revised form 19 May 2017
Accepted 20 June 2017
Available online 6 July 2017

Keywords:
Ground penetrating radar (GPR)
Non-destructive testing (NDT)
Pavement
Delamination
Time-frequency analysis

ABSTRACT

Identification of delamination in pavement layers using ground penetrating radar (GPR) is still challenging due to its limited range resolution. This paper investigates the characteristics of the composite reflection from the air-filled delamination between pavement layers by time-frequency analysis. We firstly simulated GPR data from an asphalt pavement model with an embedded air gap of different thicknesses by the Green's function method. Then we conducted a laboratory experiment on a delaminated asphalt pavement model. Both the numerical and laboratory experiment results demonstrate that both the peak instantaneous frequency and its amplitude are sensitive to the variation of the air gap thickness. When the thickness of the air gap is smaller than a quarter of the dominant wavelength, the peak instantaneous frequency of the composite reflection is higher than that of the normal interface reflection. We conclude that we can identify the delamination from the overall rise in the peak instantaneous frequency.

1. Introduction

Ground penetrating radar (GPR) has been used as a routine tool for non-destructive inspection of highway and airport pavements [1]. GPR applications for pavement evaluation include layer thickness estimation [2], the localization of the in-built reinforcement [3], crack detection [4], moisture and density estimation [5], detecting delamination between pavement layers [6], and etc. Among these applications, the most important and reliable information that can be gained from GPR measurements is the thickness estimation of pavement layers [2,7]. When the pavement layer is thick relative to the GPR pulse width, its thickness can be accurately estimated from the time delay of the reflection from its top and bottom interfaces, along with the known dielectric permittivity of the medium [8], and the relative error, which mainly comes from the velocity estimation error, is usually below 5% [9,10]. Air-coupled GPR systems are commonly used for pavement inspection due to its advantage of avoiding traffic interruption and higher resolution compared with ground-coupled GPR systems [11]. The resolution of a GPR pulse is determined by its bandwidth [12], which is mainly constrained by the GPR antenna [13]. For

* Corresponding author.
E-mail address: feng.han@xmu.edu.cn (F. Han).

http://dx.doi.org/10.1016/j.conbuildmat.2017.06.132
0950-0618/

example, an air-coupled horn antenna with a nominal frequency of 2 GHz commonly used for asphalt pavement inspection is able to identify an asphalt layer of thickness less than 25 mm [14]. In this paper, we investigate the delamination between pavement layers due to debonding or stripping. Debonding occurs when there is inadequate tack and stripping develops when there is a lack of chemical or thermal compatibility between asphalt and concrete materials [15]. However, the delamination between pavement layers is usually less than 1 cm [16,17] and can be considered a thin layer for GPR. Thus, GPR characterization of a pavement delamination is challenging.

The reflection from a thin layer is actually the superposition of the top and bottom reflection, as well as the inner multiple reflections between the top and bottom boundary of the thin layer [17,18]. A number of techniques have been proposed to enhance the GPR performance in measuring thin pavement layers or delamination. High resolution can be achieved by using a stepped-frequency GPR system with an ultra-wideband (UWB) antenna [19]. Deconvolution is applied to compress the GPR wavelet and improve its resolution for predicting pavement thin layer thickness [20–23]. Hilbert spectrum analysis of GPR data is demonstrated to be able to resolve a thin layer of $\lambda_d/8$, where λ_d is the wavelength of the dominant frequency of a GPR pulse [24]. Subspace methods exhibit super-resolution for thin-pavement thickness estimation when the signal-to-noise ratio is high [25]. However, these time-domain techniques cannot resolve an air-filled delamination between pavement layers, of which the thickness is usually in mm scale.

Frequency spectrum can provide extra information about the subsurface target. For instances, the frequency peak shift of a GPR spectrum towards a lower frequency is highly related with a high soil moisture [26,27]. From numerical simulations, it is shown that GPR traces recorded over finely laminated sequences shift towards higher frequency and spectral analysis can be used to detect super-thin layers [28,29]. In this paper, we investigate the characteristics of GPR reflection from a delamination between asphalt pavement layers through time-frequency analysis. This paper is organized as follows. The second section presents the asphalt pavement model with an embedded air-filled delamination and the theory of time-frequency analysis method. The third section gives the simulated GPR dataset associated with different delamination thickness and the results of time-frequency analysis. Results of a series of laboratory measurements over a layered pavement model are shown in the fourth section. Discussion and conclusion are given in the last section.

2. Material and method

2.1. Asphalt pavement model

As shown in Fig. 1, an asphalt pavement is usually inspected by GPR using an air-coupled horn antenna, which operates over an UWB and provides high resolution for thickness estimation of asphalt layers. The height from the antenna to the pavement surface is usually less than half a meter. This means that the pavement is still in the near field of the GPR antenna and plane wave approximation is not accurate enough. Thus, it is necessary to use a three-dimensional (3D) simulation to accurately analyze the electromagnetic response of the layered pavement structure under the radar illumination. In this circumstance, the GPR antenna can be simplified as a point source at its apparent phase center [30,31].

In practice, a highway or airport pavement structure usually consists of an asphalt layer, a base layer made of concrete and a sub-base layer consists of gravel and sand from top to bottom [8]. The asphalt layers are generally divided into a surface course, an intermediate course and a base course with different kinds of mixture. Normally each course has thickness ranges in approximately 4–6 cm and the surface course has larger permittivity as it contains the highest density and quality materials [32]. Thus, we use a layered model of asphalt pavement in the following numerical experiments. As illustrated in Fig. 2, the three asphalt layers have a thickness of 4 cm, 5 cm and 6 cm, and relative dielectric permittivity of 3.4, 3.2 and 3.0 from top to bottom [33]. We consider an air-filled delamination (air gap) between the asphalt layer and the concrete base in this study.

Fig. 1. GPR inspection of an asphalt pavement using an air-coupled TEM horn antenna.

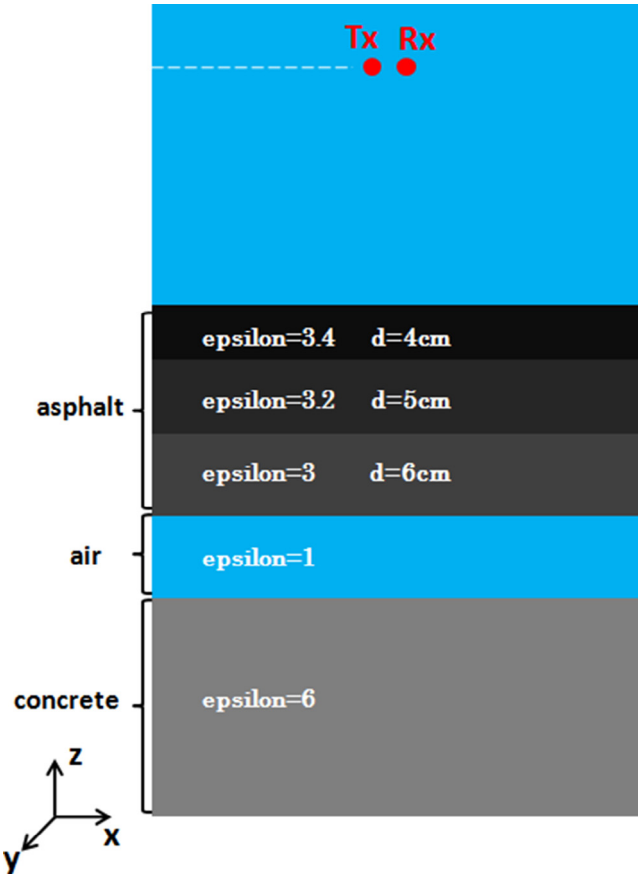

Fig. 2. Model for GPR detection of air-filled delamination inside an asphalt pavement structure.

2.2. Time-frequency analysis method

Time-frequency analysis is a powerful signal processing technique to extract unique information on scattering mechanisms. Short-time Fourier transform (STFT) is a kind of fast Fourier transformation method for this kind of analysis. Compared with the S-Transform [34], STFT performs faster. STFT is basically a sliding window Fourier transformation in time domain. As the window is shifted, a two dimensional (2D) time-frequency image is obtained by [35]

$$S(\tau,\omega) = \int f(t)g(t-\tau)e^{-j\omega t}dt \tag{1}$$

where $g(t)$ is a time window function and ω is the angular frequency. The processing is to slide the center of window to time τ, window the input signal $f(t)$ and compute the Fourier transform of the result. In this paper, a user-defined hamming window is used as $g(t)$. The length of the time window is a critical parameter in STFT. In the following numerical simulations and laboratory experiments, the time window are set to be approximately double the time duration of the dominant wavelet.

3. Numerical experiments

3.1. Green's function for GPR simulation

In order to precisely analyze the wave property of the reflection from the air gap, we perform numerical experiments at first. The most straightforward numerical method is the full wave simulation commonly conducted by finite difference time domain (FDTD) method. However, it cannot avoid the numerical dispersion error when the discretization is not dense enough. In these studies, we have to model the air gap in millimeter thickness, it leads to unaffordable computation cost by a conventional FDTD algorithm. This issue can be solved by utilizing a modified FDTD algorithm [36], which is however not easy to be implemented. In this paper, we will use the dyadic Green's function (DGF) in the layered medium. As is shown in Fig. 2, the signal at the receiver is acquired by the convolution between the signal at the transmitter and the DGF in the circumstance of the layered medium. Because the layered DGF is expressed in the frequency domain, the convolution is actually implemented by the multiplication in the frequency domain and then inversely Fourier transformed back to the time domain.

If only the electric current source is considered, the relationship between DGFs and the electric field can be expressed as [37]

$$\vec{E}(\vec{r}) = \int \underline{\underline{G}}^{EJ}(\vec{r}-\vec{r}')\cdot\vec{J}(\vec{r}')d\vec{r}' \tag{2}$$

where $\vec{r}$ denotes the field point and $\vec{r}'$ represents an arbitrary point in the volume source current $\vec{J}$. The DGF $\underline{\underline{G}}^{EJ}$ is a second order tensor and the superscript EJ means it links the electric current source $\vec{J}$ and the electric field $\vec{E}$. $\underline{\underline{G}}^{EJ}$ is expressed in frequency domain. It is actually derived from the spectrum domain. The detailed derivation is given in [37]. In most situations, the layered DGFs are in the forms of Sommerfeld integrals [38]. Numerical integration is needed to acquire the final values. If the transmitter antenna can be approximated to be a point source, the integral in Eq. (2) will disappear and it can be written in a more specific form as

$$\begin{bmatrix} E_x \\ E_y \\ E_z \end{bmatrix} = \begin{bmatrix} G^{EJ}_{xx} & G^{EJ}_{xy} & G^{EJ}_{xz} \\ G^{EJ}_{yx} & G^{EJ}_{yy} & G^{EJ}_{yz} \\ G^{EJ}_{zx} & G^{EJ}_{zy} & G^{EJ}_{zz} \end{bmatrix} \begin{bmatrix} J_x \\ J_y \\ J_z \end{bmatrix} \tag{3}$$

where J_x, J_y and J_z represent the three components of the current density of the point source in the position of $\vec{r}'$.

Before we apply the layered DGFs, we verify their accuracy by comparing them to 3D FDTD simulation results. The domain dimension for the 3D FDTD is 0.5 m × 0.5 m × 0.95 m. We use the layer configuration shown in Fig. 2 and set the thickness of the air gap to zero. The source is polarized in the $\hat{y}$ direction and its waveform at the transmitter has a Blackman-Harris window (BHW) wavelet [39] with a center frequency of 2 GHz. Fig. 3 shows the source waveform and the normalized frequency spectrum. We sample the spectrum at a step of 7.5 MHz and substitute these values into Eq. (3) (only for $J_y, J_x = J_z = 0$) and compute the electric field values.

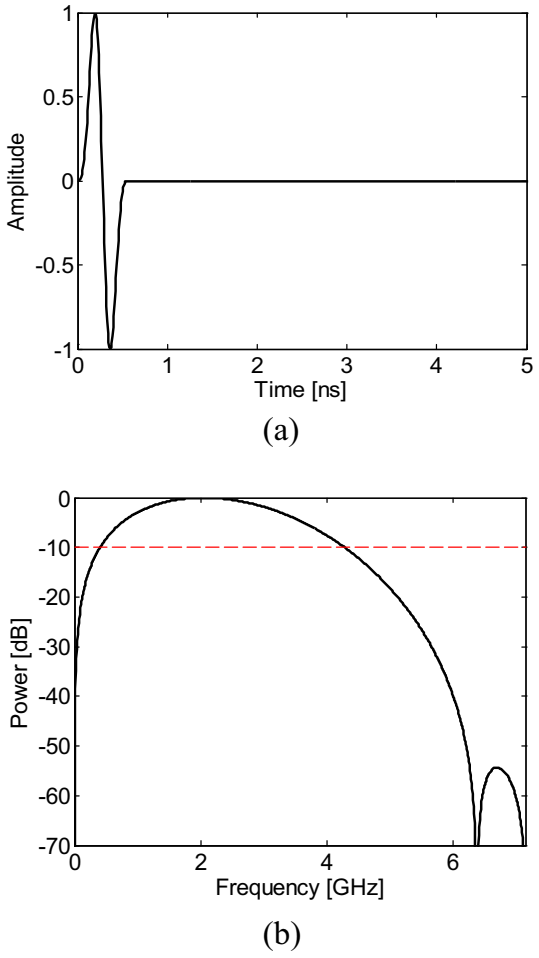

Fig. 3. (a) BHW source wavelet for GPR simulation and (b) its normalized frequency spectrum.

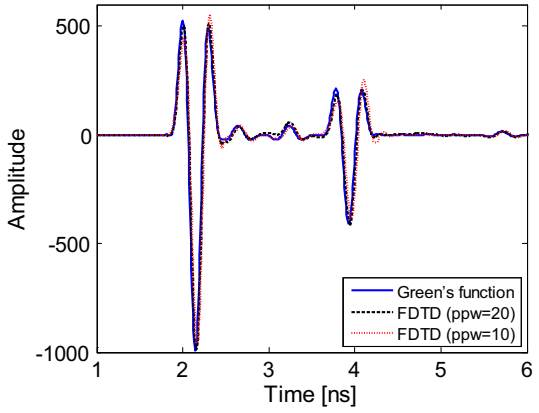

Fig. 4. Simulated GPR signal over the asphalt pavement model in Fig. 2 when the air gap is zero (no delamination). The air coupling between the transmitter and receiver has been removed.

Fig. 4 shows the comparisons of E_y between FDTD simulation results from Wavenology, a commercial software from Wave Com-

putation Technologies, Inc. (WCT), and layered DGF results. When implementing a FDTD simulation, we have to discretize the simulation space. To eliminate the numerical dispersion and ensure an acceptable accuracy, the discretization step should be at least smaller than one tenth of the smallest wavelength of the propagating electromagnetic fields, i.e. the sampling points per wavelength (PPW) should be larger than 10 [40].

We can see that the DGF results match the FDTD simulation results better when PPW is 20. The simulation time of FDTD is about one hour when PPW = 10 (dx = dy = dz = 2 mm) while 14 h when PPW = 20 (dx = dy = dz = 1 mm). However, the computation time when we use the layered DGF for all of the sampled frequencies is only several seconds.

3.2. Simulation results

A series of numerical simulations are conducted on the pavement model shown in Fig. 2 using the Green's function method. The thickness of the air gap is gradually changed from zero to 12 cm. A point source and receiver are placed 28 cm above the asphalt surface and their offset is set to 5 cm. We use a BHW source with a center frequency of 2 GHz. Theoretically the wavelength is expressed as:

$$\lambda_d = v \cdot \tau_p \tag{4}$$

where τ_p is the pulse width and v is the propagation velocity in the air gap, i.e. the velocity in vacuum. However, it is not easy to accurately determine the duration of the pulse when it is overlapped with the neighboring signals and contaminated by noise in the real GPR data. So we use the effective bandwidth to define its wavelength, as expressed by:

$$\lambda_d = v/B \tag{5}$$

where the effective bandwidth B is defined as the span between the high and low frequency limits where the magnitude of the spectrum is 10 dB weaker than that of the peak frequency [41], which is indicated by the dash line in Fig. 3(b). Due to the wavelet distortion and frequency dependent attenuation of electromagnetic waves during propagation in real measurement, the effective bandwidth of the GPR pulse can be decreased as it travels. Therefore, we use the wavelet of the reflection from the top of the air gap when its thickness is zero to define the dominant wavelength in the following numerical and laboratory experiments.

Fig. 5 shows a portion of the simulation results after coupling removal, which highlights the variation of the reflection from the embedded air gap while its thickness increases. When the gap thickness is zero, there is a reflection from the interface between the asphalt and concrete, which is extracted by a user-defined hamming window in Fig. 5(a) and would be used for the calculation of dominant wavelength λ_d. From the frequency spectrum of this windowed reflection wavelet, the effective bandwidth is estimated to be 2.77 GHz and the dominant wavelength is calculated to be 10.8 cm by Eq. (5) in this case. With a small gap thickness less than $\lambda_d/4$ (e.g. 2.7 cm), we can hardly distinguish the top and bottom reflection and can only observe a composite reflection pulse, of which the amplitude and phase is changing with the increasing thickness. When the gap thickness grows larger than $\lambda_d/2$ (e.g. 6 cm, 8 cm, 10 cm and 12 cm), the top and bottom reflection from the embedded air gap, which are opposite in polarity, can be clearly identified. Apparently, one can hardly distinguish the gap thickness merely by judgment from the reflective pulse amplitude and phase in time domain when air gap is smaller than $\lambda_d/4$.

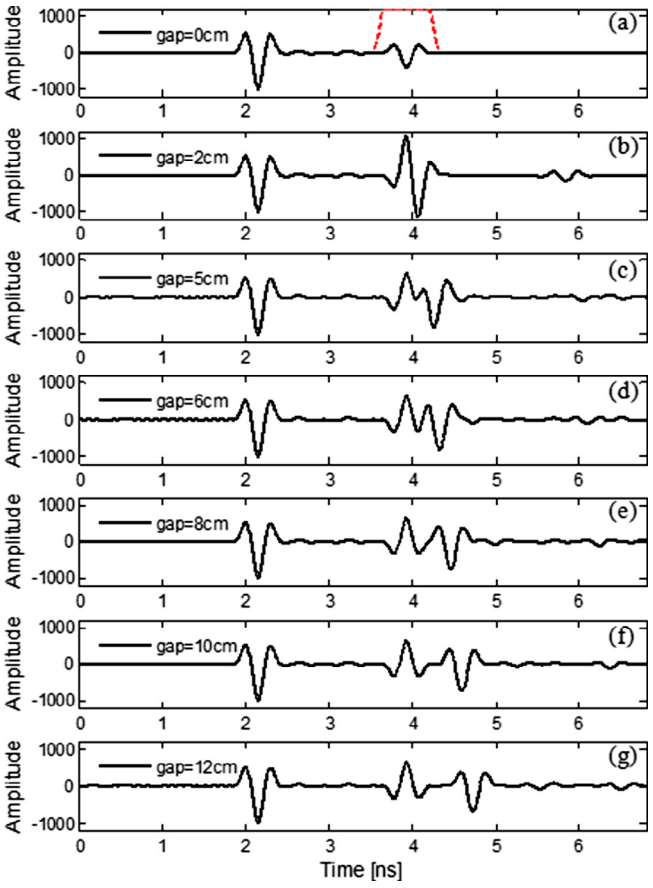

Fig. 5. Simulated GPR signals over the asphalt pavement model in Fig. 2 when the air gap is 0 cm, 2 cm, 5 cm, 6 cm, 8 cm, 10 cm and 12 cm respectively. The air coupling between the transmitter and receiver has been removed. The reflection from the embedded air gap arrives at about 3.6 ns.

3.3. Results of time-frequency analysis

STFT is applied to the simulated GPR data to obtain more valuable information about the delamination and the results are shown in Fig. 6. If we find the maximum-amplitude point in each time-frequency spectrum and extract the column data passing through this point, which is indicated by the white dash line in Fig. 6, we can obtain the instantaneous frequency spectrum of air gap reflection. The results are shown in Fig. 7. With a small gap thickness less than $\lambda_d/4$ (e.g. 0 cm and 2 cm), we can observe a single peak in the instantaneous frequency spectrum. When the gap thickness grows larger than $\lambda_d/4$ (e.g. 5 cm and 8 cm), multiple peaks appear. However, when the gap thickness is large enough relative to λ_d (i.e. thicker than 10 cm), only one peak is depicted instead of more peaks. We plot the peak frequencies and their corresponding amplitude in the instantaneous frequency spectrum versus the gap thickness in Figs. 8 and 9, respectively.

In Fig. 8, we can see that there is a single peak frequency above the transverse dotted line when the thin gap thickness is less than $\lambda_d/4$. With the gap thickness approaches zero, the peak frequency of the gap reflection is approximately equal to the peak frequency of interface reflection without gap. The value of peak frequency rises with the increase of gap thickness and reaches a maximum at the position of 0.7 cm, then drops with increasing thickness. When the gap thickness is $\lambda_d/4$, the peak frequency returns to the value of that without an air gap. When the thickness is larger than $\lambda_d/4$, there are double peak frequencies, with the primary peak frequency below the transverse dotted line and the secondary peak frequency twice as high as the primary one. Both peak fre-

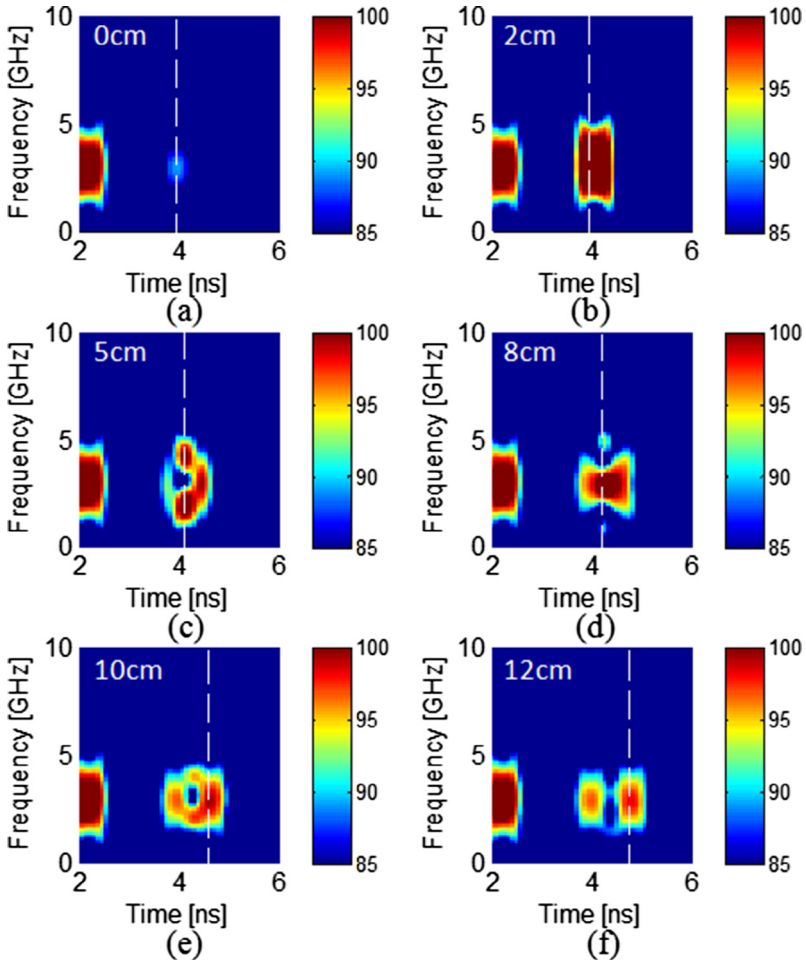

Fig. 6. Time-frequency representation of simulated GPR signal over the asphalt pavement model in Fig. 2 when the air gap is (a) 0 cm, (b) 2 cm, (c) 5 cm, (d) 8 cm, (e) 10 cm and (f) 12 cm respectively.

quencies are dropping with the increase of gap thickness. When the thickness is larger than $\lambda_d/2$, a third peak frequency approximately three times as high as the primary one arises. All of the three peak frequencies are dropping with the increase of gap thickness. However, when the gap is large enough relative to λ_d, the peak frequency keeps the same as that of the interface reflection. This is because the reflections from the top and base of the air gap are well separated, which could not be covered by the sliding window used in the STFT. The above observations can be summarized into a formula as

$$\begin{cases} n=1, f_{p1} > f_d: & 0 < h < \frac{\lambda_d}{4} \\ n=2, f_{p1} = \frac{f_{p2}}{2} < f_d: & \frac{\lambda_d}{4} < h < \frac{\lambda_d}{2} \\ n=3, f_{p1} = \frac{f_{p2}}{2} = \frac{f_{p3}}{3} < f_d: & \frac{\lambda_d}{2} < h < \frac{3\lambda_d}{4} \end{cases} \quad (6)$$

where n denotes the number of frequency peaks, f_{p1}, f_{p2} and f_{p3} indicate the first, second and third peak frequency in an instantaneous frequency spectrum respectively, f_d indicates the peak frequency of the interface reflection and h is the gap thickness.

In Fig. 9, we can see that the amplitude of the primary peak frequency reaches a maximum value when the gap thickness is close to $\lambda_d/4$, and the amplitudes of the first two peak frequencies are equal when the gap thickness is close to $\lambda_d/2$.

The occurrence of the multiple frequency peaks and their shift with the varying gap thickness in the instantaneous frequency spectrum can be explained using the interference models in Fig. 10. Due to the opposite sign of the reflection coefficient on the top and bottom interfaces of the embedded air gap, the bottom reflection and its multiples are out of phase from the top reflection when the air gap thickness is close to zero. When the gap thickness equals to a quarter of the wavelength, the phase change of the bottom reflection is π due to the two-way traveling inside the air gap. Therefore, the top and bottom reflection interfere constructively with each other at the corresponding frequency, and the first frequency peak occurs. When the thickness increases, the peak frequency shifts towards a lower frequency, which corresponds to a longer wavelength. Similar explanations apply for the second and third frequency peaks when the gap thicknesses equal to one eighth and one sixteenth wavelength, respectively.

In the case that the gap thickness is less than $\lambda_d/4$, which is the most common one in an asphalt pavement structure [16,17], the peak frequency is higher than the peak frequency of the interface reflection without an air gap, and its trend shows an arc. It is difficult to quantitatively estimate the gap thickness from the value of the peak frequency. Nevertheless, we can detect the existence of a delamination (air gap) from the shift of the peak frequency towards a higher value compared with that of the interface reflection without a delamination.

4. Laboratory experiments

4.1. Data acquisition

To validate the results of the numerical simulation, a laboratory experiment was conducted. The experimental configuration is shown in Fig. 11. 40 pieces of gypsum plaster boards were used

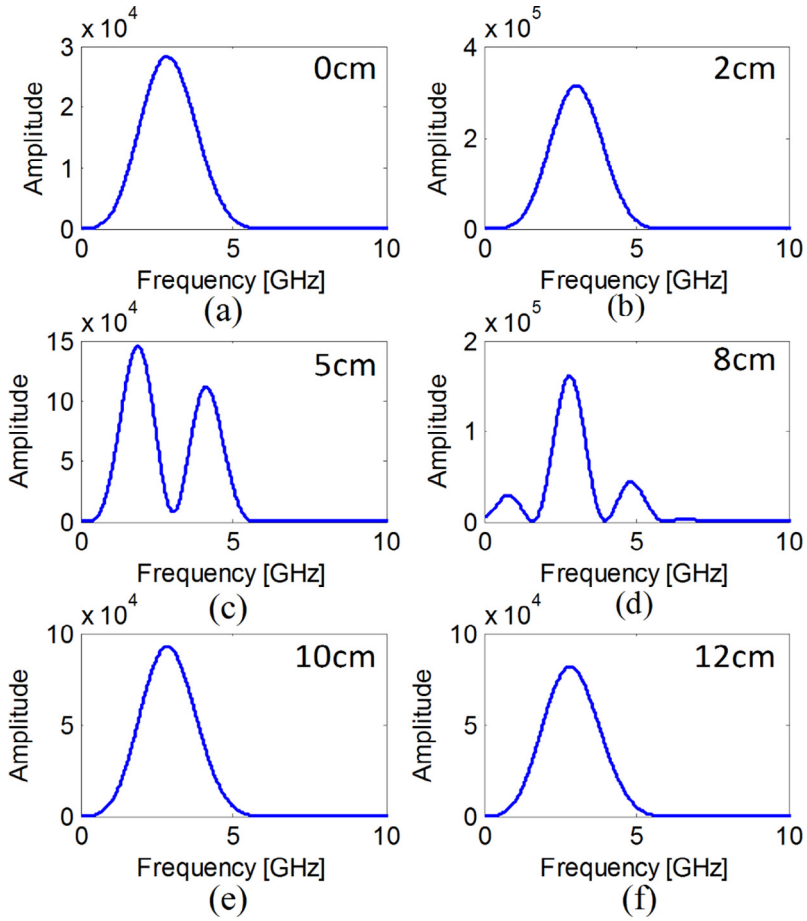

Fig. 7. Instantaneous frequency spectrums of simulated GPR reflection signals from the embedded air gap, of which thickness is (a) 0 cm, (b) 2 cm, (c) 5 cm,(d) 8 cm, (e) 10 cm and(f) 12 cm, respectively, at its arrival time.

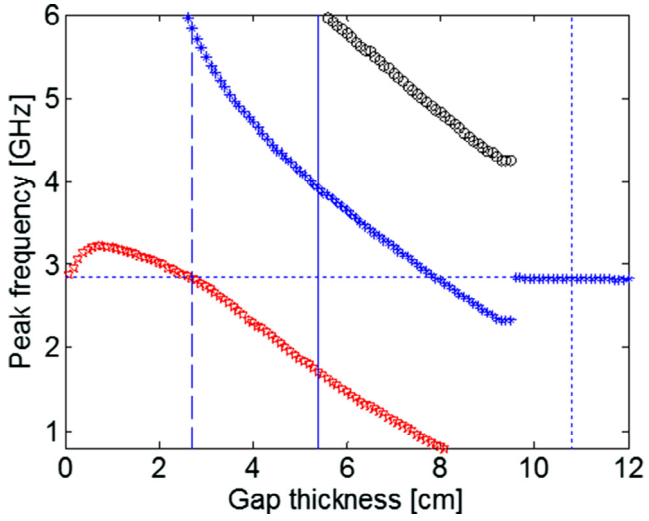

Fig. 8. Peak frequencies of the instantaneous spectrum of the simulated GPR reflection signal from the embedded air gap. The square, asterisk and circle signs represent the primary, secondary and third peak frequency, respectively. The transverse dotted line indicates the location of the peak frequency of the interface reflection in Fig. 7(a), which equals to 2.84 GHz in this case. The vertical dash line, solid line and dotted line indicate the location of $\lambda_d/4$, $\lambda_d/2$ and λ_d of the interface reflection in Fig. 5(a).

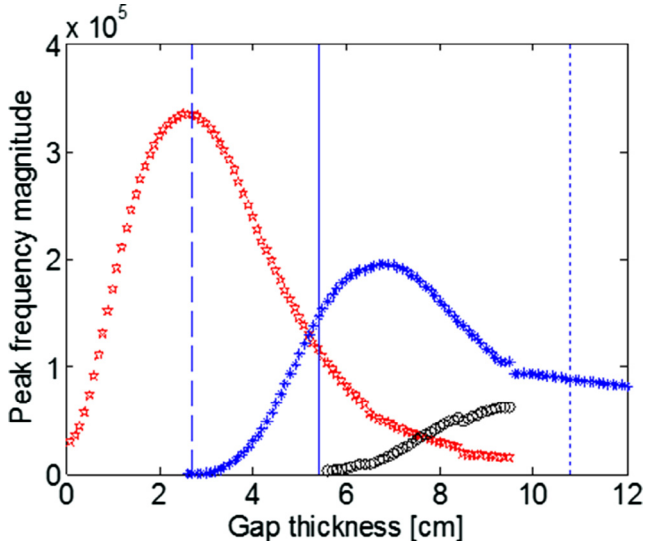

Fig. 9. Amplitude of the peak frequencies shown in Fig. 8. The square, asterisk and circle signs represent the primary, secondary and third peak frequency, respectively. The vertical dash line and solid line indicate the location of $\lambda_d/4$ and $\lambda_d/2$ of the interface reflection in Fig. 5(a).

to model the asphalt layer, since gypsum has similar dielectric properties as the asphalt medium [7]. Different numbers of foam boards were inserted in the middle to imitate the delamination (air gap) with a series of thicknesses. GPR measurement was carried out by means of a stepped-frequency system which consists of a vector network analyzer (VNA) and a horn antenna (SATIMO

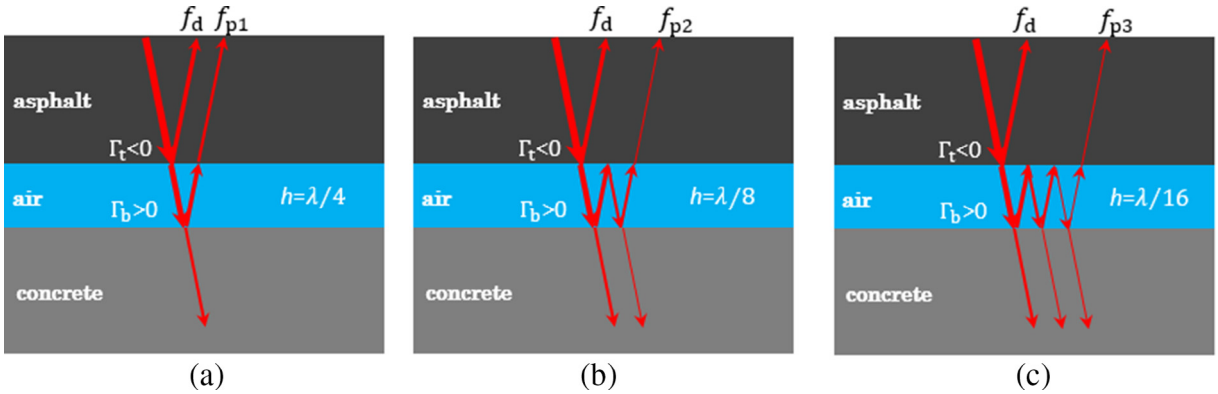

Fig. 10. Models for explanation of the occurrence and shift of the frequency peaks. The first (a), second (b) and third (c) peaks occur when the gap thickness equals to a quarter, one eighth and one sixteenth of the corresponding wavelength, respectively.

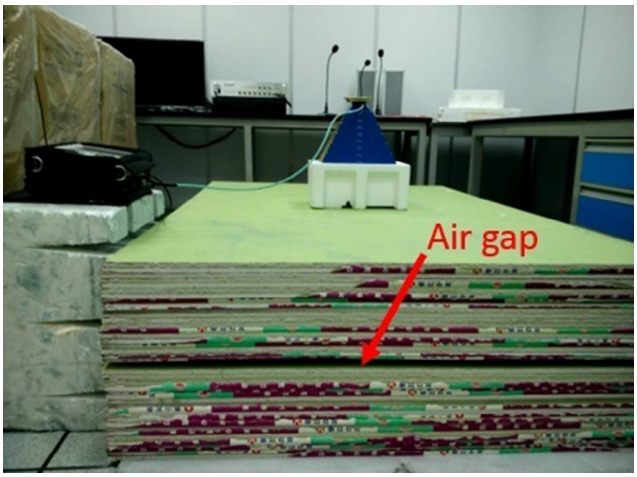

Fig. 11. Laboratory GPR measurement on a pavement model using a TEM horn antenna. The delamination (air gap) is modelled by inserting thin foam layers between gypsum boards.

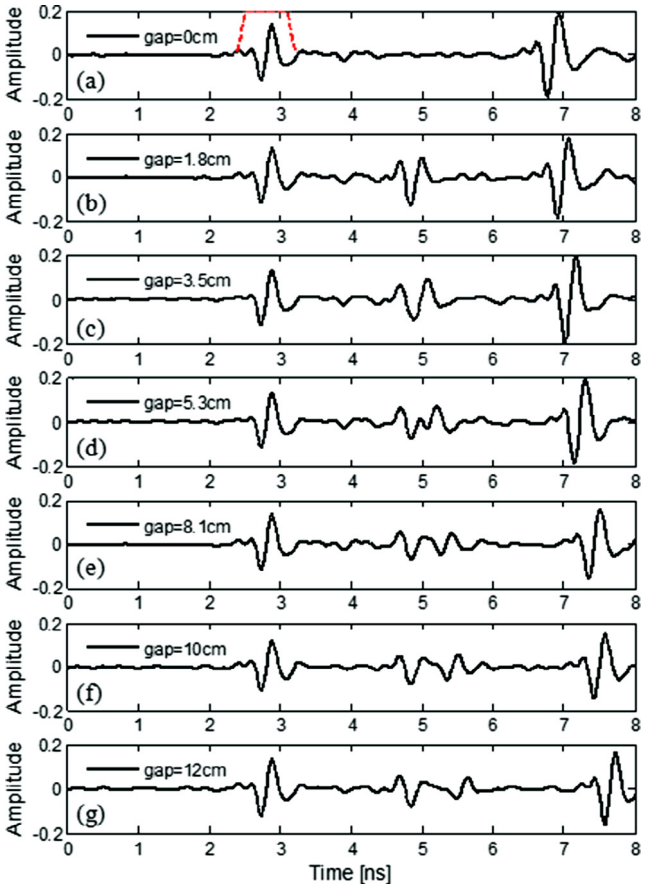

Fig. 12. Measured GPR signal over the asphalt pavement model in Fig. 11 when the air gap is 0 cm, 1.8 cm, 3.5 cm, 5.3 cm, 8.1 cm, 10 cm and 12 cm respectively. The air coupling has been removed by a background measurement.

SH800 dual ridge horn 0.8–12 GHz). The height of the feeding point on the horn antenna is about 35 cm above the gypsum surface, and the sweep frequency ranges from 0.06 to 6 GHz. The horn antenna was used as the transmitter, as well as the receiver. A background measurement was also conducted by pointing the antenna upward in the air to remove the strong reflection at antenna feeding point.12 sets of tests are conducted with the gap thickness of 0 cm, 0.8 cm, 1.3 cm, 1.8 cm, 2.8 cm, 3.5 cm, 5.3 cm, 6.2 cm, 7.2 cm, 8.1 cm, 10 cm and 12 cm. A reference reflection wavelet from the air/gypsum interface was recorded in the test with the 0 cm gap thickness, which is extracted by a time window in Fig. 12(a) and is used for the calculation of the dominant wavelength, which equals 12.7 cm in this case.

4.2. Results

Fig. 12 shows seven examples of the measured GPR data after background removal in time domain. The pulse arising at about4.6 ns is the reflection from the air gap, while the latter pulse at about 6.7 ns is the reflection from the metallic ground. As in the numerical experiments, STFT is applied on the measured time domain GPR signal and the peak frequencies of the instantaneous spectrum of the air gap reflection are extracted. The peak frequencies versus the gap thickness are plotted in Fig. 13.

It is observed from Fig. 13 that when the air gap thickness is less than $\lambda_d/4$, there is a single frequency peak, which is higher than of the interface reflection. If the air gap thickness approximates $\lambda_d/4$ (3.2 cm in this case), its peak frequency is close to the peak frequency of the surface reflection. When the air gap thickness is greater than $\lambda_d/4$ ($\lambda_d/2$), the secondary (third) peak frequency arises and keeps dropping with the increased thickness. When the gap is large enough relative to λ_d (i.e. 12 cm), where the reflections from the top and base of the air gap are completely separated, the peak frequency equals to that of the interface reflection. From

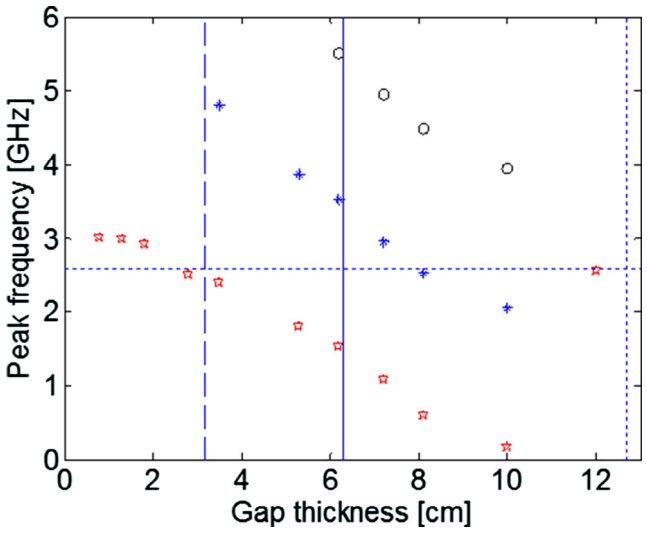

Fig. 13. Peak frequencies of the instantaneous spectrum of measured GPR reflection signal from the embedded air gap in Fig. 10. The square, asterisk and circle signs represent the primary, secondary and third peak frequency, respectively. The transverse dotted line indicates the location of the peak frequency of the air/surface reflection in Fig. 12(a), which equals to 2.58 GHz in this case. The vertical dash line, solid line and dotted line indicate the location of $\lambda_d/4$, $\lambda_d/2$ and λ_d of the surface reflection in Fig. 11(a).

these measurement results, we can see that the relation between the peak frequencies and the air gap thickness is quite similar to the simulated data. This verifies that the time frequency analysis is a valuable method for identification of delamination (air gap) between pavement layers.

5. Discussion and conclusion

In this paper, we investigate the characteristics of the composite reflection from the air-filled delamination between pavement layers by time-frequency analysis, which is implemented by STFT. Numerical simulation of a 3D asphalt pavement model with different air gap thicknesses was conducted to obtain the GPR responses using the Green' function method, which is demonstrated to yield higher accuracy and computational efficiency, compared with the conventional FDTD method. A laboratory experiments was also conducted. STFT is applied to both the numerical and laboratory data. Both results demonstrate that both the peak instantaneous frequency and its amplitude are sensitive to the variation of the air gap thickness. When the thickness of the air gap is smaller than $\lambda_d/4$, the peak instantaneous frequency of the composite reflection is higher than that of the interface reflection (without an air gap). As for the case when thickness of the gap is larger than $\lambda_d/2$, it is easy to identify the gap by observing the time delay between the reflections such that there is no need for time-frequency analysis. It is worth to note that all of the observations in this research are valid only for the STFT approach of time-frequency analysis mentioned in this paper, and the results are based on specific wavelengths and air gap model we used in this work. If a different model or a different center frequency is used, we suggest to perform similar simulations and time-frequency analysis.

In practice, the delamination between asphalt pavement layers is usually in a mm scale, smaller than $\lambda_d/4$, The shift of a GPR spectrum peak towards a higher frequency can be useful for detection of the delamination in situ GPR inspection. From the view of the practical application, a careful calibration of the peak instantaneous frequency of the reference interface reflection (without an air gap) should be carried out before the field GPR measurement. Then we can identify the presence of the delamination between pavement layers from the overall rise in the peak instantaneous frequency of the layer reflection. Nevertheless, the quantitative characterization of the delamination thickness, which is in millimeter scale, is still a challenging issue.

Acknowledgements

This research study was supported in part by National Natural Science Foundation of China (41504111), the Fundamental Research Funds for the Central Universities, Xiamen University (No. 20720150083) and Guangxi Science and Technology Development Funds (2015BC17047).

References

[1] T. Saarenketo, T. Scullion, Road evaluation with ground penetrating radar, J. Appl. Geophys. 43 (2000) 119–138, http://dx.doi.org/10.1016/S0926-9851(99)00052-X.
[2] M. Solla, H. Lorenzo, J. Martínez-Sánchez, V. Pérez-Gracia, Applications of GPR in association with other non-destructive testing methods in surveying of transport infrastructures, in: A. Benedetto, L. Pajewski (Eds.), Civil Engineering Applications of Ground Penetrating Radar, Springer, 2015, pp. 327–342, http://dx.doi.org/10.1007/978-3-319-04813-0_13.
[3] J. Stryk, R. Matula, K. Pospisil, Possibilities of ground penetrating radar usage within acceptance tests of rigid pavements, J. Appl. Geophys. 97 (2013) 11–26, http://dx.doi.org/10.1016/j.jappgeo.2013.06.013.
[4] L. Krysiński, J. Sudyka, GPR abilities in investigation of the pavement transversal cracks, J. Appl. Geophys. 97 (2013) 27–36, http://dx.doi.org/10.1016/j.jappgeo.2013.03.010.
[5] Z. Leng, I.L. Al-Qadi, S. Lahouar, Development and validation for in situ asphalt mixture density prediction models, NDT E Int. 44 (2011) 369–375, http://dx.doi.org/10.1016/j.ndteint.2011.03.002.
[6] L. Krysiński, J. Sudyka, Typology of reflections in the assessment of the interlayer bonding condition of the bituminous pavement by the use of an impulse high- frequency ground-penetrating radar, Non-Destr. Test. Eval. 27 (2012) 219–227, http://dx.doi.org/10.1080/10589759.2012.674525.
[7] H. Liu, M. Sato, In situ measurement of pavement thickness and dielectric permittivity by GPR using an antenna array, NDT E Int. 64 (2014) 65–71, http://dx.doi.org/10.1016/j.ndteint.2014.03.001.
[8] I.L. Al-Qadi, S. Lahouar, Measuring layer thicknesses with GPR – theory to practice, Constr. Build. Mater. 19 (2005) 763–772, http://dx.doi.org/10.1016/j.conbuildmat.2005.06.005.
[9] A. Loizos, C. Plati, Accuracy of pavement thicknesses estimation using different ground penetrating radar analysis approaches, NDT E Int. 40 (2007) 147–157, http://dx.doi.org/10.1016/j.ndteint.2006.09.001.
[10] A. Loizos, C. Plati, Accuracy of ground penetrating radar horn-antenna technique for sensing pavement subsurface, IEEE Sens. J. 7 (2007) 842–850, http://dx.doi.org/10.1109/JSEN.2007.894152.
[11] A. Benedetto, F. Tosti, L. Bianchini Ciampoli, F. D'Amico, An overview of ground-penetrating radar signal processing techniques for road inspections, Signal Process. 132 (2016) 1–9, http://dx.doi.org/10.1016/j.sigpro.2016.05.016.
[12] A.P. Annan, Ground penetrating radar, in: D.K. Butler (Ed.), Near-Surface Geophysics, Society of Exploration Geophysicists, 2005, pp. 357–434.
[13] F.I. Rial, M. Pereira, H. Lorenzo, P. Arias, A. Novo, Resolution of GPR bowtie antennas: an experimental approach, J. Appl. Geophys. 67 (2009) 367–373, http://dx.doi.org/10.1016/j.jappgeo.2008.05.003.
[14] J. Stryk, A.M. Alani, R. Matula, K. Pospisil, Innovative inspection procedures for effective GPR surveying of critical transport infrastructures (pavements, bridges and tunnels), in: Civil Engineering Applications of Ground Penetrating Radar, 2015, pp. 71–95, doi:10.1007/978-3-319-04813-0_3.
[15] M. Heitzman, K. Maser, N.H. Tran, R. Brown, H. Bell, S. Holland, H. Ceylan, K. Belli, D. Hiltunen, Nondestructive Testing to Identify Delaminations Between HMA Layers, Alabama, 2013, doi:10.17226/22768.
[16] Z. Dong, S. Ye, Y. Gao, G. Fang, X. Zhang, Z. Xue, T. Zhang, Rapid detection methods for asphalt pavement thicknesses and defects by a vehicle-mounted ground penetrating radar (GPR) system, Sensors (Switzerland) 16 (2016) 1–18, http://dx.doi.org/10.3390/s16122067.
[17] V.D.W. Andrey, Characterization of Thin Layers into Concrete with Ground Penetrating Radar, University of Liege, 2014.
[18] M.B. Widess, How thin is a thin bed?, Geophysics 38 (1973) 1176–1180, http://dxdoi.org/10.1190/1.1440403.
[19] X. Dérobert, C. Fauchard, P. Côte, E. Le Brusq, E. Guillanton, J. Dauvignac, C. Pichot, Step-frequency radar applied on thin road layers, J. Appl. Geophys. 47 (2001) 317–325, http://dx.doi.org/10.1016/S0926-9851(01)00075-1.
[20] J. Xia, E.K. Franseen, R.D. Miller, T.V. Weis, Application of deterministic deconvolution of ground-penetrating radar data in a study of carbonate strata, J. Appl. Geophys. 56 (2004) 213–229, http://dx.doi.org/10.1016/j.jappgeo.2004.07.003.

[21] N. Economou, A. Vafidis, H. Hamdan, G. Kritikakis, N. Andronikidis, K. Dimitriadis, Time-varying deconvolution of GPR data in civil engineering, Nondestr. Test. Eval. 27 (2012) 285–292, http://dx.doi.org/10.1080/10589759.2012.695787.
[22] S. Zhao, P. Shangguan, I.L. Al-Qadi, Application of regularized deconvolution technique for predicting pavement thin layer thicknesses from ground penetrating radar data, NDT E Int. 73 (2015) 1–7, http://dx.doi.org/10.1016/j.ndteint.2015.03.001.
[23] S. Zhao, I.L. Al-Qadi, Development of regularization methods on simulated ground-penetrating radar signals to predict thin asphalt overlay thickness, Signal Process. 132 (2017) 261–271, http://dx.doi.org/10.1016/j.sigpro.2016.06.015.
[24] X.W. Zhang, Y.Z. Gao, G.Y. Fang, Application of Hilbert spectrum analysis in ground penetrating radar thin layer recognition, Chin. J. Geophys. 56 (2013) 2790–2798, http://dx.doi.org/10.6038/cjg20130827.
[25] C. Le Bastard, V. Baltazart, Y. Wang, J. Saillard, Thin-pavement thickness estimation using GPR with high-resolution and superresolution methods, IEEE Trans. Geosci. Remote Sens. 45 (2007) 2511–2519, http://dx.doi.org/10.1109/TGRS.2007.900982.
[26] A. Benedetto, Water content evaluation in unsaturated soil using GPR signal analysis in the frequency domain, J. Appl. Geophys. 71 (2010) 26–35, http://dx.doi.org/10.1016/j.jappgeo.2010.03.001.
[27] F. Tosti, A. Benedetto, L. Bianchini Ciampoli, S. Lambot, C. Patriarca, E.C. Slob, GPR analysis of clayey soil behaviour in unsaturated conditions for pavement engineering and geoscience applications, Near Surf. Geophys. 14 (2016) 127–144, http://dx.doi.org/10.3997/1873-0604.2016011.
[28] S. Guha, S.E. Kruse, E.E. Wright, U.E. Kruse, Spectral analysis of ground penetrating radar response to thin sedimentary layers, Geophys. Res. Lett. 32 (2005) L23304, http://dx.doi.org/10.1029/2005GL023933.
[29] S. Guha, S. Kruse, P. Wang, Joint time-frequency analysis of GPR data over layered sequences, Leading Edge 27 (2008) 1454–1460, http://dx.doi.org/10.1190/1.3011017.
[30] H. Liu, M. Sato, Determination of the phase center position and delay of a Vivaldi antenna, IEICE Electron. Express 10 (2013) 1–7, http://dx.doi.org/10.1587/elex.10.20130573.
[31] K.Z. Jadoon, S. Lambot, E.C. Slob, H. Vereecken, Analysis of horn antenna transfer functions and phase-center position for modeling off-ground GPR, IEEE Trans. Geosci. Remote Sens. 49 (2011) 1649–1662, http://dx.doi.org/10.1109/TGRS.2010.2089691.
[32] J. Garcia, K. Hansen, HMA Pavement Mix Type Selection Guide, National Asphalt Pavement Association and Federal Highways Administration, Lanham, 2001.
[33] D.J. Daniels, Ground Penetrating Radar, second ed., IEE, London, 2004.
[34] R.G. Stockwell, L. Mansinha, R.P. Lowe, Localization of the complex spectrum: the S transform, IEEE Trans. Signal Process. 44 (1996) 998–1001, http://dx.doi.org/10.1109/78.492555.
[35] A. Majkowski, Marcin Kołodziej, R.J. Rak, Joint time-frequency and wavelet analysis-an introduction, Metrol. Meas. Syst. XXI (2014) 741–758, http://dx.doi.org/10.2478/mms-2014-0054.
[36] M.K. Kärkkäinen, Subcell FDTD modeling of electrically thin dispersive layers, IEEE Trans. Microwave Theory Tech. 51 (2003) 1774–1780, http://dx.doi.org/10.1109/TMTT.2003.812584.
[37] K.A. Michalski, J.R. Mosig, Multilayered media Green's functions in integral equation formulations, IEEE Trans. Antennas Propag. 45 (1997) 508–519, http://dx.doi.org/10.1109/8.558666.
[38] K.A. Michalski, Extrapolation methods for sommerfeld integral tails, IEEE Trans. Antennas Propag. 46 (1998) 1405–1418, http://dx.doi.org/10.1109/8.725271.
[39] Y.H. Chen, W.C. Chew, M.L. Oristaglio, Application of perfectly matched layers to the transient modeling of subsurface EM problems, Geophysics 62 (1997) 1730–1736, http://dx.doi.org/10.1190/1.1444273.
[40] A. Giannopoulos, Modelling ground penetrating radar by GprMax, Constr. Build. Mater. 19 (2005) 755–762, http://dx.doi.org/10.1016/j.conbuildmat.2005.06.007.
[41] H. Liu, X. Xie, K. Takahashi, M. Sato, Groundwater level monitoring for hydraulic characterization of an unconfined aquifer by common mid-point measurements using GPR, J. Environ. Eng. Geophys. 19 (2014) 259–268, http://dx.doi.org/10.2113/JEEG19.4.xx.